Automated detection of a prostate Ni-Ti stent in electronic portal images.

Carl, Jesper Hansen; Nielsen, Henning; Nielsen, Jane; Lund, B.; Larsen, E.H.

Published in:
Medical Physics

Publication date:
2006

Document Version
Publisher's PDF, also known as Version of record

Automated detection of a prostate Ni–Ti stent in electronic portal images

Jesper Carl[a)]
Department of Medical Physics, Aalborg Hospital, University of Aarhus, Aalborg, Denmark

Henning Nielsen
Computer Vision and Media Technology Laboratory (CVMT), Aalborg University, Aalborg, Denmark

Jane Nielsen
Department of Medical Physics, Aalborg Hospital, University of Aarhus, Aalborg, Denmark

Bente Lund
Department of Oncology, Aalborg Hospital, Aalborg, Denmark

Erik Hoejkjaer Larsen
Department of Urology, Aalborg Hospital, Aalborg, Denmark

(Received 23 December 2005; revised 26 September 2006;
accepted for publication 28 September 2006; published 20 November 2006)

Planning target volumes (PTV) in fractionated radiotherapy still have to be outlined with wide margins to the clinical target volume due to uncertainties arising from daily shift of the prostate position. A recently proposed new method of visualization of the prostate is based on insertion of a thermo-expandable Ni–Ti stent. The current study proposes a new detection algorithm for automated detection of the Ni–Ti stent in electronic portal images. The algorithm is based on the Ni–Ti stent having a cylindrical shape with a fixed diameter, which was used as the basis for an automated detection algorithm. The automated method uses enhancement of lines combined with a grayscale morphology operation that looks for enhanced pixels separated with a distance similar to the diameter of the stent. The images in this study are all from prostate cancer patients treated with radiotherapy in a previous study. Images of a stent inserted in a humanoid phantom demonstrated a localization accuracy of 0.4–0.7 mm which equals the pixel size in the image. The automated detection of the stent was compared to manual detection in 71 pairs of orthogonal images taken in nine patients. The algorithm was successful in 67 of 71 pairs of images. The method is fast, has a high success rate, good accuracy, and has a potential for unsupervised localization of the prostate before radiotherapy, which would enable automated repositioning before treatment and allow for the use of very tight PTV margins. © *2006 American Association of Physicists in Medicine*.
[DOI: 10.1118/1.2369466]

Key words: malignant, neoplasm, prostate, radiotherapy, localization, portal imaging

I. INTRODUCTION

Increased doses in external beam radiotherapy (EBRT) of localized prostate cancer increase local control although increased survival rate has not yet been shown.[1] Organs at risk in prostate cancer patients treated with EBRT are bladder and rectum. The use of modern imaging techniques and three-dimensional (3D) conformal treatment planning may reduce the volume of normal tissue irradiated.[2–4] When normal tissue volume is reduced, evidence of consequently reduced toxicity exists, even with increased dose to the prostate.[5] Even further reduction of normal tissue volume in the high dose region may be possible using intensity modulated radio therapy.[6] Planning target volume (PTV) in fractionated EBRT, however, still has to be outlined with wide margins to the Clinical Target Volume due to geometrical uncertainties. Uncertainties arise from shift in daily prostate position due to variation in bladder and rectal filling[7,8] and setup errors. Daily variations in the position of the prostate are in the range 10–20 mm.[9] Errors may be even greater for patients in prone position due to movements caused by respiration.[10,11]

Various methods have been developed to reduce PTV margins. These methods are based on indirect visualization of the prostate using x-ray or electronic portal imaging devices (EPIDs). Visualization can be done using radio opaque implanted 2–5 mm gold (Au) markers.[9,12–15] Automated detection of the markers will facilitate daily clinical use. Several algorithms such as template matching,[16] marker extraction kernels[17] and Mexican hat filtering[18] have been investigated for automated detection of gold markers. Detection success rate is between 85% and 100%[17–19] and positioning accuracy within 1–2 mm.[17,19] Image noise, bony structures and air cavities reduce the detection success rate of gold markers.[17,19] Recently a new method of visualization of the prostate has been proposed, which is based on insertion of a thermo-expandable Ni–Ti stent (Memokath®, Engineers and Doctors) in the prostatic urethra. The Memokath stent was developed for treatment of bladder outlet obstruction in patients with benign prostate hyperplasia.[20] The stent is visible on electronic portal images from an amorphous silicon imager (Varian as500) and can be positioned with the same accuracy as gold markers. In the present study a new detec-

FIG. 1. The thermo-expandable Ni–Ti stent is shown together with insertion kit to mount over the flexible cystoscope. Initially the stent is a straight cylinder. The stent shown here has been flushed using water at 60 °C. This causes the collar to expand at the lower end of the stent. The expanded collar locks the stent position in the prostate.

tion algorithm suited for automated positioning of the Ni–Ti stent is proposed based on a fixed 3D shape and dimension of an inserted stent. The algorithm is using a gray scale morphology operation that looks for enhanced pixels within a given distance equal to the stent diameter. The present study investigated the feasibility of automated detection using this new algorithm to look for a Ni–Ti stent in portal images.

II. MATERIAL AND METHODS

The images in this study are all from patients included in a previous study.[21] All patients presented with histological verified local or locally advanced prostate cancer (stage pT2b to pT3b, N0, M0; UICC 1992 classification was used) were all candidates for intended curative radiotherapy. The stent used in the study is shown in Fig. 1. The stent is made of a coiled Ni–Ti wire and has a cylindrical shape. External and internal diameters of the cylinder are 8.0 and 6.7 mm respectively, i.e., a wall thickness of 0.65 mm. The collar has an expanded maximal external diameter of 13 mm. Because of the cylindrical shape of the stent, the distance of Ni–Ti wire traversed by a beam orthogonal to the cylinder axis is rising from 0 at the external diameter to 4.3 mm when the beam is tangential to the internal diameter as shown in Fig. 2. The average distance traversed by the beam is around 3 mm. This is equivalent to an approximately 4% contrast enhancement. Consequently, the cylindrical shape is imaged as two parallel lines with higher than background absorption. The physical pixel size of the Varian as500 imager is 0.784 mm/pixel. This was scaled to the isocenter using the accelerator source to axis distance and source to detector distance, which are read from the dicom header in each individual image. This gave a pixel size of approximately 0.56 mm in the isocenter, but dependent on the actual position of the imager. Treatment was given with an isocenter 3D conformal treatment plan including three multi leave collimator fields (one anterior and two lateral wedged fields). Pairs of orthogonal 15 cm $\times$ 15 cm isocenter setup fields (anterior and lateral projections) were used to obtain electronic portal images in eight treatment sessions in each patient (session numbers 1, 2, 3, 6, 11, 21, 22 and 23). Electronic portal images were recorded using a Varian As500 electronic portal imaging device (EPID). The acquisition protocol was the Varian standard protocol, i.e., the image was averaged over four frames taken with 6 MV using in total between 3 and 5 MU. The orthogonal images were used to determine the 3D reference position of the stent. The stent position was calculated manually using the orthogonal reconstruction in the Brachyvision® program which is part of the Eclipse® dose planning system from

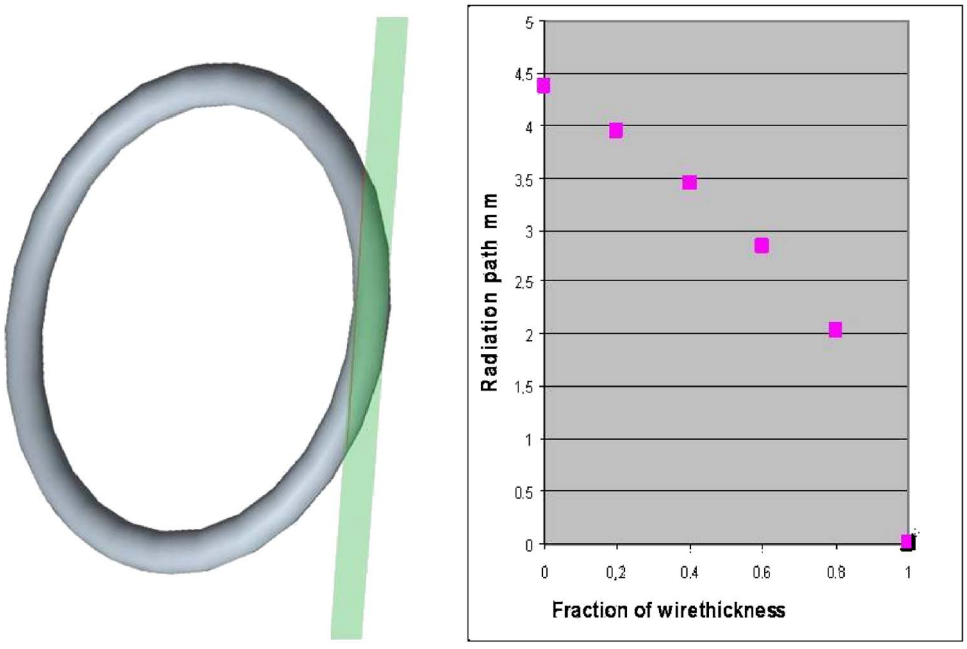

FIG. 2. The figure demonstrates to the right the calculated radiation pathway through a coil in the Ni–Ti stent as shown to the left. The longest pathway is observed when the ray is tangential to the inner diameter of the coil. The pathway decreases to zero as the ray become tangential to the outer diameter of the coil.

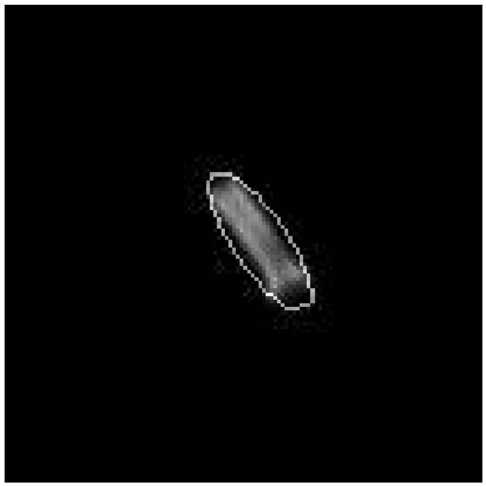

FIG. 3. Lateral DRR image showing the stent only and its bounding ellipsoid. The major axis of the bounding ellipsoid is used to determine rotation.

Varian. All images were analyzed with both the manual and the new automated method. The manually determined 3D position of the stent was used as reference for the automated algorithm. Precision of the manual method was also estimated using double readings. In order to estimate localization accuracy a number of images were taken of a Ni–Ti stent placed in a humanoid phantom (Alderson). The stent was inserted in cranial-caudal (CC) direction as a hole was drilled in consecutive slices of the Alderson phantom. The phantom was computer tomography scanned and a treatment plan including setup fields analogous to that used in real patients was made. The phantom was placed on the accelerator couch. The couch was then moved to predefined positions using the readout of couch position. The position of the stent was subsequently determined using the automated method on sets of orthogonal images taken after each couch movement.

A. Automated detection algorithm

The automated algorithm is based on enhancement of vertical lines, followed by a morphology erosion, binary threshold and finally extraction of the largest particle. All image processing is done in ImageJ.[22] Before enhancement of vertical lines the portal image was rotated until the cylindrical axis of the stent was vertical. The angle of rotation was initially determined for both the anterior and lateral projection using digital reconstructed radiograms (DRRs) in each patient. DRRs were created in beams eye view in the planning system (Eclipse®) with the stent visible only, i.e., bones were not reconstructed. The stent was segmented in the DRR using maximum entropy in the multi threshold plug in written for ImageJ. An ellipsoid is fitted and the angle of rotation is determined from the orientation of the major axis of the ellipsoid as shown in Fig. 3. The angle was stored and used for rotation of subsequent portal images. After rotation of each portal image the cylindrical axis of the stent would be vertical within plus or minus 20°, irrespectively of variations in daily prostate rotation. Histogram normalization was done for each portal image followed by a convolution with a 5×5 kernel to enhance vertical lines. The 5×5 kernel used is

$$\begin{matrix} -1 & 0 & 2 & 0 & -1 \\ -1 & 0 & 2 & 0 & -1 \\ -1 & 0 & 2 & 0 & -1 \\ -1 & 0 & 2 & 0 & -1 \\ -1 & 0 & 2 & 0 & -1 \end{matrix}$$

This convolution enhances line structures that are vertical, including the stent. The stent will show up in the images as two parallel enhanced lines typically 12–13 pixels apart, and each of the lines 1–2 pixels wide. Following the convolution a grayscale morphology operation is performed using the grayscale morphology plug in ImageJ. The plug in performs a gray level erosion using a structure element consisting of two points with a horizontal distance equal to the fixed diameter of the stent [see inset in Fig. 4(b)]. Subsequently a binary threshold of the eroded image is done using maximum entropy in the multi threshold plug in written for ImageJ. Finally a particle analysis is run on the threshold image. The particle analysis looks for eight neighbor pixels, all to be part of the same particle. All particles touching the edge of the image are excluded. The largest particle is then extracted. Center of gravity for the largest particle is used as representation point of the stent. The automated detection is done separately for both images in each pair of orthogonal images. The coordinate of the stent representation point is calculated relative to the image center (beam axis). The beam axis is also determined in each portal image. A binary threshold value equal to 20% the maximal grayscale value in the portal images is set. This value is chosen to make the beam portal appear white and the remaining detector area black. The beam axis is set equal to the center of gravity of the white area. The 3D coordinates are then calculated from the two two-dimensional projections using a previously published method for localization of implants from biplane radiographs.[23] The automated method is characterized as being successful in an image pair if the difference between stent position coordinates deviates less than 2 mm from the same coordinates determined using the manual method in both images. All image processing is done using Java plug in's and macros in the image processing toolbox ImageJ from National Institute of Health.

III. RESULTS

Localization accuracy was tested placing a Ni–Ti stent in a humanoid phantom (Alderson). The results from this test are shown in Table I. The difference between the couch position and the position determined with the algorithm was not statistically different from 0 for either the left-right (LR) or the anterior-posterior (AP) positions. For the cranial-caudal (CC) coordinate there was a significant difference. In general the test demonstrated a localization accuracy of 0.4–0.7 mm (one standard deviation), which was approximately equal to the EPID detector pixel size in the isocenter. A systematic difference of 0.8 mm was, however, observed in the CC di-

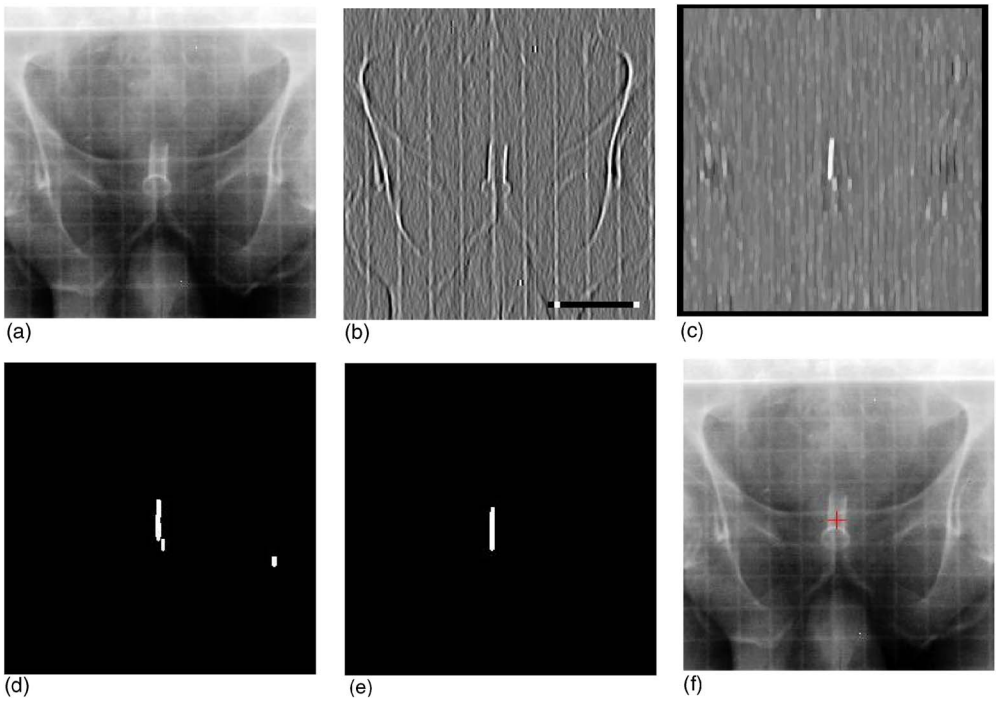

FIG. 4. The figure demonstrates the various steps in the automated detection algorithm used: (a) The original electronic portal image enhanced using histogram equalizations; (b) line enhancement using 5×5 filtering. Small inset is an enlarged diagram of the morphology structure element. White dots are one pixel in the structure elements; (c) Grayscale morphology operation leaving only bright pixels with a distance equal to the diameter of the stent; (d) binary threshold of image using maximum entropy; (e) result from eight neighbor particle analysis selecting the largest particle; (f) Center of gravity from the largest particle in image; (e) is marked with a red cross on image (a).

rection. Precision of the manual method was determined from double readings and demonstrated to be less than 0.4 mm. Patient images from nine patients were analyzed using the automated method. The images were acquired in eight different treatment sessions for each patient. In total, 71 pairs of orthogonal images were acquired (one pair was missing).[21] Initially automated detection was attempted applying template match analysis (data not shown). The template match analysis was, however, critically dependent on a correct shape, alignment and scaling of template and image. Thus the template match analysis did not provide the same success rate as the grayscale morphology algorithm. The various steps in the automated method are demonstrated Fig. 3. The automated method on average took less than 0.5 s to determine the position of the stent in an image. Comparison of the 3D coordinates determined with both the manual and new algorithm is shown in Fig. 5, and a good correspondence between the (LR), (AP) and (CC) coordinates is seen.

TABLE I. Localization of Ni–Ti stent placed in Alderson humanoid phantom. The table shows mean and standard deviation of difference between couch coordinate and coordinate determined by the algorithm.

	LR	AP	CC
Mean (mm)	0,1	0,3	0,8
StdErr (mm)	0,4	0,7	0,4

From the calculated differences in Table II it can be seen that no statistical difference between the manual and automated method was observed. Localization accuracy of the automated method was shown to be in the range of 0.4–0.7 mm. Analogously the differences between the manual and automated method in patient images demonstrated standard deviations of 0.3–0.8 mm, equal to 1–2 pixels. Apparently the LR and AP coordinates demonstrate the smallest differences. From Table II it can be seen that the automated method failed in four cases, i.e., the differences between manual and automated detection were larger than the success criteria of 2 mm. However, differences larger than 5 mm were only seen in one case (highly deteriorated image).

IV. DISCUSSION

A new automated detection of a Ni–Ti stent inserted into the prostate was developed. The method was successfully applied to detect the position of the Ni–Ti stent in portal images. Detection of a thin metal marker in portal images is difficult. The detection is made difficult by high noise level, low contrast and background structures such as bony edges or air cavities. This new method takes advantage of the stents cylindrical shape with a fixed diameter to overcome the low signal and high noise ratio in portal images. Failure was characterized as the difference between the manual and automated detection of more than 2 mm. The automated localization method failed in four cases. The detection failed completely in one lateral image of very poor quality (portal

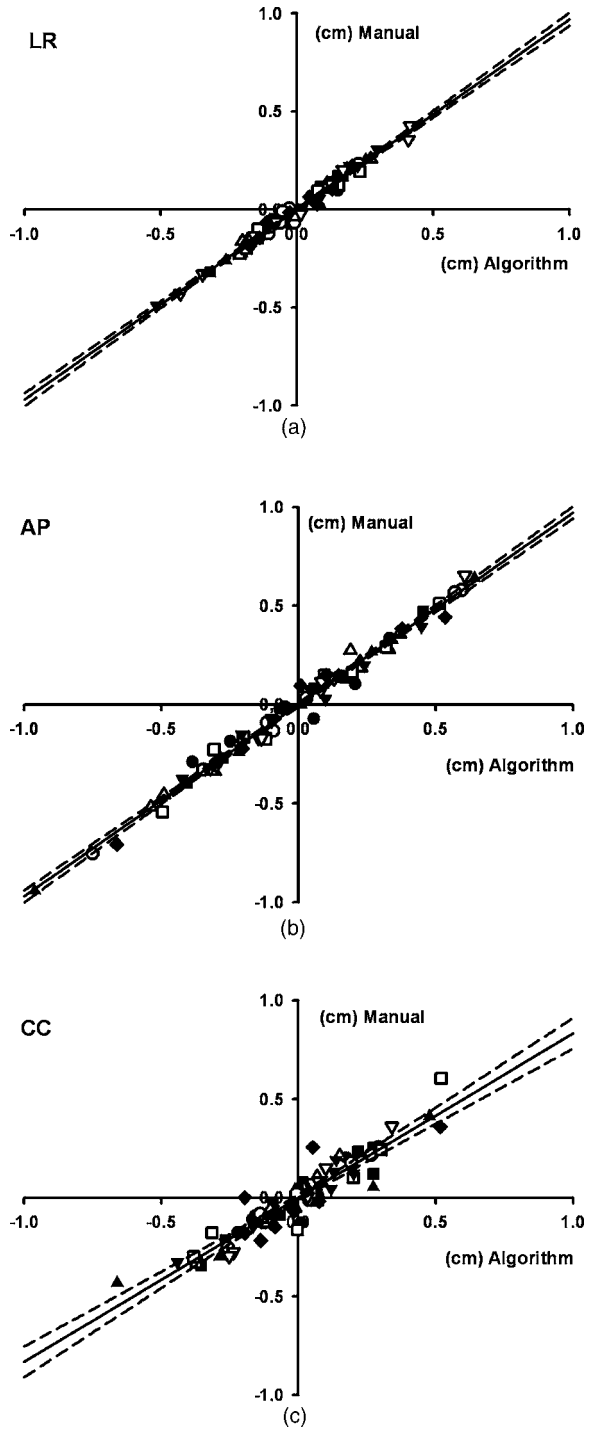

FIG. 5. Results of localization of a Ni–Ti stent using both a manual and the new algorithm (automated method). Results are from 71 image pairs taken in different treatment sessions of nine different patients. Each patient is represented by a symbol. The position of the stent is shown in three separate plots defined using the three directions: (a) LR (left-right) (b) AP (anterior-posterior) and (c) CC (cranial-caudal). Also shown in each plot are the regression line and its 95% confidence limits.

TABLE II. Mean and standard deviation of difference between manual and automated detection of stent coordinates. The three coordinates are determined from 71 pairs of orthogonal portal images. The last two rows are number of image pairs in which the difference is greater than 2 mm, but less than 5 mm and greater than 5 mm, respectively. The AP and CC differences in the last row occurred in the same image. The image was taken with a defect imager.

	LR	AP	CC
Mean (mm)	0.0	0.0	0.0
StdDev (mm)	0.3	0.4	0.8
>2 mm	0	0	3
>5 mm	0	1	1

imager defect) giving a difference larger than 5 mm. In total the method has yielded acceptable results in 67 of 71 image pairs (94%). The algorithm is susceptible to errors in the angle of rotation. Deviation from a vertical position of the stent may introduce variation in line enhancement. This in turn can lead to discontinuities of the gray values representing the stent and breakup of the particle during threshold. Another source of error can be the carbon fiber net of the linac treatment couch. The net may be enhanced as well as the stent. Part of the enhanced net can erroneously combine with part of the stent collar and be detected as part of the cylindrical shape. Because the couch net is a regular structure it may theoretically be removed using fact Fourier transform to filter out the frequency of the net. But in other cases bony structures combined with part of the stent collar. In such cases filtering in the Fourier domain would not solve the problem. In total, however, the algorithm was shown to be robust. Even when large variations in exposure were seen and different imagers were used. Differences between the manual and automated method larger than 2 mm do occur in images from several patients but only in the CC direction. Thus a lower precision in the CC coordinate seems to be a general weakness of the automated method and is observed in both phantom and patient images. It seems that the method has a low precision detecting the ends of the stent. As a consequence, extension or reduction of the detected stent may occur in one or both ends of the stent. This may lead to a shift primarily in the CC coordinate. This shift is, however, minimized because the CC coordinate is averaged over coordinates from two orthogonal images. The automated method may improve if both ends of the stent can be detected with greater precision. One way to check whether both stent ends have been detected correctly would be to calculate the total length of the stent from the detected end points. Checking the length of the stent would be important as criteria for stopping the algorithm, if the automated method is allowed to run unsupervised. The localization accuracy was demonstrated in the phantom pictures of this study to be equal to the size of 1 pixel. The accuracy of the algorithm was observed to be similar in patient images, even though this also includes the accuracy of the manual method as well. The present study is consistent with other studies using gold markers, which report an accuracy of 0.2–0.6 mm.[17,18] Their accuracy was also determined on a phantom, but with a portal imager having a better resolution than the one used in the present study. Another study[19] also reports an accuracy similar to the present study. Here analysis was done on a large number of clinical images and with a resolution of the imag-

ing system equivalent to the one used in this study. The algorithm in the present study was reasonably fast. Fast enough for use in clinical routine if only the setup has to be done before treatment in each session. If real time tracking of the stent should be done with the electronic portal imaging detector, time resolution has to be improved. The method in its present form has not been optimized. The coding of the algorithm may be improved. Furthermore, the search area may be limited for the following images, when the position of the stent has been determined in the first image. This may lead to an even faster version of the algorithm. In the case of real time tracking the algorithm may actually not be the major obstacle. It may be the portal imager itself. At the moment acquisition time for our Varian as500 imager is in seconds. The acquisition time may be reduced if a protocol that yields images with a poorer signal to noise ratio is allowed. In an attempt to optimize the time/resolution factor we are currently testing the influence of increased noise on the performance of the algorithm. But even so, the acquisition time may be too long for real time tracking. Future improvement in the as500 imager may lead to both reduced acquisition time and improved resolution. Both would improve the proposed algorithm's potential for real time tracking. Currently we are also investigating the potential for improvement of the algorithm in terms of a better accuracy especially in the direction along the axis of a cylindrical object. A totally different approach would be using kV x-ray images for tracking instead of high voltage images. The detection algorithm would then be able to be run on images with a much better contrast to noise ratio. Consequently, the automated method would be expected to detect the ends of the stent with a higher precision. All together there is a potential for this new algorithm for positioning of patients before radiotherapy and even in the field of tracking and respiration gating.

V. CONCLUSION

Using a Ni–Ti stent to visualize the prostate, a new automated detection algorithm has been presented. This method has been successfully applied to portal images. The method has been demonstrated to have a high success rate, a good accuracy and a potential for unsupervised localization of the prostate before radiotherapy. This new method would enable automated repositioning before treatment and allow for the use of very tight PTV margins. The method has a future potential for real time tracking of respiration movements.

[a]Author to whom correspondence should be addressed. Electronic mail: jcarl@aas.nja.dk

[1]O. Algan *et al.*, "Is there a subset of patients with PSA > =20 ng/ml who do well after conformal beam radiotherapy?," Radiat. Oncol. Invest. **7**, 106–110 (1999).

[2]J. M. Michalski *et al.*, "Preliminary report of toxicity following 3D radiation therapy for prostate cancer on 3DOG/RTOG 9406," Int. J. Radiat. Oncol., Biol., Phys. **46**, 391–402 (2000).

[3]P. Bey *et al.*, "Dose escalation with 3D-CRT in prostate cancer: French study of dose escalation with conformal 3D radiotherapy in prostate cancer - Preliminary results," Int. J. Radiat. Oncol., Biol., Phys. **48**, 513–517 (2000).

[4]L. J. Boersma *et al.*, "Estimation of the incidence of late bladder and rectum complications after high-dose (70–78 GY) conformal radiotherapy for prostate cancer, using dose-volume histograms," Int. J. Radiat. Oncol., Biol., Phys. **41**, 83–92 (1998).

[5]D. P. Dearnaley *et al.*, "Comparison of radiation side effects of conformal and conventional radiotherapy in prostate cancer: A randomized trial," Lancet **353**, 267–272 (1999).

[6]B. S. Teh *et al.*, "Clinical experience with intensity-modulated radiation therapy (IMRT) for prostate cancer with the use of rectal balloon for prostate immobilization," Med. Dosim **27**, 105–113 (2002).

[7]C. J. Beard *et al.*, "Analysis of prostate and seminal vesicle motion: Implications for treatment planning," Int. J. Radiat. Oncol., Biol., Phys. **34**, 451–458 (1996).

[8]H. Alasti *et al.*, "Portal imaging for evaluation of daily on-line setup errors and off-line organ motion during conformal irradiation of carcinoma of the prostate," Int. J. Radiat. Oncol., Biol., Phys. **49**, 869–884 (2001).

[9]E. Vigneault *et al.*, "Electronic portal imaging device detection of radioopaque markers for the evaluation of prostate position during megavoltage irradiation: A clinical study," Int. J. Radiat. Oncol., Biol., Phys. **37**, 205–212 (1997).

[10]L. A. Dawson *et al.*, "A comparison of ventilatory prostate movement in four treatment positions," Int. J. Radiat. Oncol., Biol., Phys. **48**, 319–323 (2000).

[11]S. Malone *et al.*, "Respiratory-induced prostate motion: Quantification and characterization," Int. J. Radiat. Oncol., Biol., Phys. **48**, 105–109 (2000).

[12]J. M. Crook *et al.*, "Prostate motion during standard radiotherapy as assessed by fiducial markers," Radiother. Oncol. **37**, 35–42 (1995).

[13]K. Kitamura *et al.*, "Registration accuracy and possible migration of internal fiducial gold marker implanted in prostate and liver treated with real-time tumor-tracking radiation therapy (RTRT)," Radiother. Oncol. **62**, 275–281 (2002).

[14]P. Fransson *et al.*, "Prospective evaluation of urinary and intestinal side effects after BeamCath stereotactic dose-escalated radiotherapy of prostate cancer," Radiother. Oncol. **63**, 239–248 (2002).

[15]P. Fransson *et al.*, "Acute side effects after dose-escalation treatment of prostate cancer using the new urethral catheter BeamCath technique," Acta Oncol. **40**, 756–765 (2001).

[16]J. M. Balter *et al.*, "Automated localization of the prostate at the time of treatment using implanted radiopaque markers: Technical feasibility," Int. J. Radiat. Oncol., Biol., Phys. **33**, 1281–1286 (1995).

[17]A. Nederveen, J. Lagendijk, and P. Hofman, "Detection of fiducial gold markers for automatic on-line megavoltage position verification using a marker extraction kernel (MEK)," Int. J. Radiat. Oncol., Biol., Phys. **47**, 1435–1442 (2000).

[18]D. Buck, M. Alber, and F. Nusslin, "Potential and limitations of the automatic detection of fiducial markers using an amorphous silicon flat-panel imager," Phys. Med. Biol. **48**, 763–774 (2003).

[19]S. Aubin *et al.*, "Robustness and precision of an automatic marker detection algorithm for online prostate daily targeting using a standard V-EPID," Med. Phys. **30**, 1825–1832 (2003).

[20]R. Kulkarni and E. Bellamy, "Nickel-titanium shape memory alloy Memokath 051 ureteral stent for managing long-term ureteral obstruction: 4-year experience," J. Urol. (Baltimore) **166**, 1750–1754 (2001).

[21]J. Carl *et al.*, "Feasibility study using a Ni–Ti stent and electronic portal imaging to localize the prostate during radiotherapy 1," Radiother. Oncol. **78**, 199–206 (2006).

[22]W. S. Rasband, "ImageJ U. S. National Institutes of Health, Bethesda, ML., http://rsb.info.nih.gov/lj/, 1997-2006."

[23]J. Cai *et al.*, "A method for more efficient source localization of interstitial implants with biplane radiographs," Med. Phys. **24**, 1229–1234 (1997).